Frequency and magnetic field dependent properties of ordered magnetic nanoparticle arrangements

Nils Neugebauer,[1, a)] Toni Hache,[2, 3] Matthias T. Elm,[1, 4, 5] Detlev M. Hofmann,[1, 4] Christian Heiliger,[4, 6] Helmut Schultheiss,[2, 7] and Peter J. Klar[1, 4]

[1)] *Institute of Experimental Physics I, Justus Liebig University Giessen, Heinrich-Buff-Ring 16, 35392 Giessen, Germany*

[2)] *Helmholtz-Center Dresden–Rossendorf, Institute of Ion Beam Physics and Materials Research, Bautzner Landstraße 400, 01328 Dresden, Germany*

[3)] *Institute for Physics, Technische University Chemnitz, 09107 Chemnitz, Germany*

[4)] *Center for Materials Research (ZfM/LaMa), Justus Liebig University Giessen, Heinrich-Buff-Ring 16, 35392 Giessen, Germany*

[5)] *Institute of Physical Chemistry, Justus Liebig University Giessen, Heinrich-Buff-Ring 17, 35392 Giessen, Germany*

[6)] *Institute for Theoretical Physics, Justus Liebig University Giessen, Heinrich-Buff-Ring 16, 35392 Giessen, Germany*

[7)] *Technische Universität Dresden, 01062 Dresden, Germany*

(Dated: xxx; Revised xxx)

We present a frequency and magnetic field dependent investigation of ordered arrangements of 20 nm magnetic nanoparticles (MNPs) consisting of magnetite (Fe_3O_4) by employing micro Brillouin light scattering microscopy. We utilized electron beam lithography to prepare hexagonally arranged, circularly shaped MNP-assemblies consisting of a single layer of MNPs using a variant of the Langmuir-Blodgett technique. By comparing the results with non-structured, layered superlattices of MNPs, further insight into the influence of size and geometry of the arrangement on the collective properties is obtained. We show that at low static external field strengths, two signals occur in frequency dependent measurements for both non-structured and structured assemblies. Enlarging the static external field strength leads to a sharpening of the main signal, while the satellite signal decreases in its intensity and increases in its linewidth. The occurrence of multiple signals at low external field strengths is also confirmed by sweeping the static external field and keeping the excitation frequency constant. Micromagnetic simulations unravel the origin of the different signals and their dependence on the static external field strength, enabling an interpretation of the observed characteristics in terms of different local environments of an MNPs forming the MNP assembly.

I. INTRODUCTION

The development and improvement of novel electronic devices employed in technological applications has driven modern science to find and unveil new approaches in preparing, e.g., novel functional units in electronic circuits or magnetic devices. In recent years, conventional fabrication processes, in which top-down and bottom-up techniques were used to create structured thin films, have been challenged by various novel experimental approaches, which utilize nanoscale components such as magnetic quantum dots or likewise nanoparticles[1–6]. Using nanoparticles as building blocks of devices yields additional degrees of freedom to manipulate the fundamental device characteristics, which is not possible using bulk materials only[7–10]. Employing colloidal quantum dots has therefore attracted great and increasing interest during the past decades, since the controllability of their shape, size, composition[11], and arrangement in highly ordered structures is steadily advancing[5,9,11–14]. The potential introduction of nanoparticles in devices for a specific application requires a detailed knowledge of the fundamental interactions of the nanoparticles with their environment. In particular in the case of magnetic nanoparticles this also includes interactions between the nano-sized constituents themselves and, thus, their collective behavior[10,15–18]. The fundamental interactions between magnetic nanoparticles are governed by dipole interactions, since the magnetic core of each particle is surrounded by an organic shell (oleic acid), which prevents an electronic contact between the particles and, thus, e.g., exchange interaction between them[19–21]. Certainly, dipole interactions between magnetic nanoparticles become more and more important as the size of the MNPs themselves and the lateral extension of their arrangement in ordered and densely packed structured superlattices decreases[22]. In the light of a continuous miniaturization of electronic circuits and magnetic devices, the finite size and the shape of the functional unit play a more important role because the surface to volume ratio increases with decreasing arrangement size. Depending on the unit's size and shape different local environments occur, which makes an understanding of details of the interaction of a magnetic moment of an MNP with its environment indispensable.

Here we present an investigation of the dipolar interaction between MNPs within circularly structured and non-structured, layered superlattices. ~~Micro~~ Brillouin light scattering (µBLS) microscopy is employed to investigate frequency and external field dependent proper-

[a)] Electronic mail: Nils.Neugebauer@physik.uni-giessen.de

ties of the corresponding nano-arrangements. On these length scales, dipole interactions between the different constituents determine the overall magnetic properties. Obtaining a deep understanding of the collective dipolar behavior of the MNP arrangements and of their response to the simultaneously applied external magnetic field and microwave field represents the motivation of this paper. Obtaining insight into the collective properties of the MNP-arrangements, micromagnetic simulations of the corresponding model systems were carried out, which enables us to the extract the internal dipole field distribution and to identify the active regions of the arrangement yielding a specific resonant excitation.

II. METHODS

A. Sample Preparation

The preparation of the ordered MNP arrangement for the µBLS experiments comprises two main fabrication steps. First, a microwave antenna is defined on an high-ohmic silicon wafer (>10.000 Ω/cm), which is later used to excite magnetic oscillations within the corresponding magnetic structure in the µBLS-experiment. For this purpose, the wafer is coated with a 300 nm thick PMMA A4 950K layer to enable patterning of the antenna by using a low dose of $D = 1.000\ \mu C/cm^2$ (at an acceleration voltage of 15 kV) during an electron beam lithography (EBL) process. When using low doses, PMMA serves as a positive resist. Thus the exposed areas are dissolved during the development process, i.e., during the immersion in an isopropanol-water-solution (volume ratio 2:1) for 45 seconds. Subsequently, a 5 nm thick chromium layer serving as an adhesion aid and a 100 nm gold layer are deposited using electron beam evaporation. The residual PMMA and metal layer are removed by placing the wafer in an ultra sonic bath filled with acetone for 10 minutes at 20° C.

Afterwards, the second fabrication step is performed. It comprises the formation of the MNP arrangement on the structured silicon wafer. Following the technique proposed by Pang[23] *et al.*, magnetite (Fe_3O_4) MNPs with an average diameter of $d_{NP} = 20$ nm suspended in toluene (standard variation $\sigma = 5$ % - particle concentration $c \sim 4.5 \cdot 10^{13}$ particles/mL - Sigma-Aldrich product number: 725366) are diluted by adding 50 parts of toluene as solvent to one part of the original suspension. In order to enable patterning of the MNPs during the EBL-exposure, five parts of 950K PMMA A4 are added to the diluted MNP-suspension. To ensure good homogeneity of the suspension, the mixture is placed in an ultrasonic bath for 10 minutes at room temperature. Subsequently 100 µL of the MNP-PMMA-toluene-mixture are pipetted onto a water subphase within a beaker of 10 cm in diameter. After 30 minutes, the solvent is entirely evaporated and a monolayer of MNPs separated by PMMA is formed. The MNP monolayer is then transferred onto a previously structured silicon wafer resulting in hexagonally arranged MNPs as shown in Fig. 1. PMMA between the individual particles can act as a negative resist when using high doses during the EBL exposure. Thus using a high dose of $D = 15.000\ \mu C/cm^2$ in a subsequent EBL process leaves behind exposed areas of the MNP monolayer which after resist development yield the structured MNP arrangement. The inset of Fig. 1 shows an example of a circular MNP arrangement with a diameter of ∼ 450 nm prepared in this fashion. Preparing non-structured, layered superlattices is achieved by increasing the concentration of MNPs in the MNP-PMMA-toluene-mixture by a factor of 2, which leads to arrangements consisting of multiple layers up to 8 layers thick.

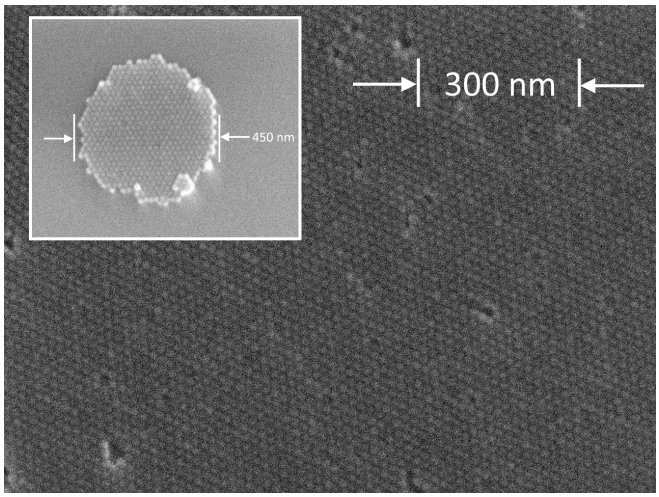

FIG. 1. Using a variant of the Langmuir-Blodgett-technique, a mixture of MNPs suspended in toluene and PMMA is pipetted onto a water subphase. During the evaporation of the solvent, a self-assembling process takes place leading to a hexagonal arrangement of a single layer of MNPs which can be transferred to a silicon wafer substrate. After the EBL-exposure with high doses and a subsequent development process, patterned MNP-arrangements can be synthesized as shown in the inset.

B. Micro Brillouin light scattering Microscopy

To investigate the dynamic properties of magnetic nano-structures, several techniques have been established to excite and detect magnetic oscillations of the corresponding magnetic structure. Among these, µBLS microscopy has demonstrated an excellent capability of investigating frequency- and external magnetic field dependent properties[18,24–26]. In the experiment, a sample is placed on a microwave antenna structure in an external magnetic field B_{ext} and the response of the magnetic system is then analyzed by exposing the sample to photons of a wavelength (/frequency) of 532 nm (/563,52 PHz). In order to stimulate magnetic oscillations within the sample, the same spot on the sample is also excited with

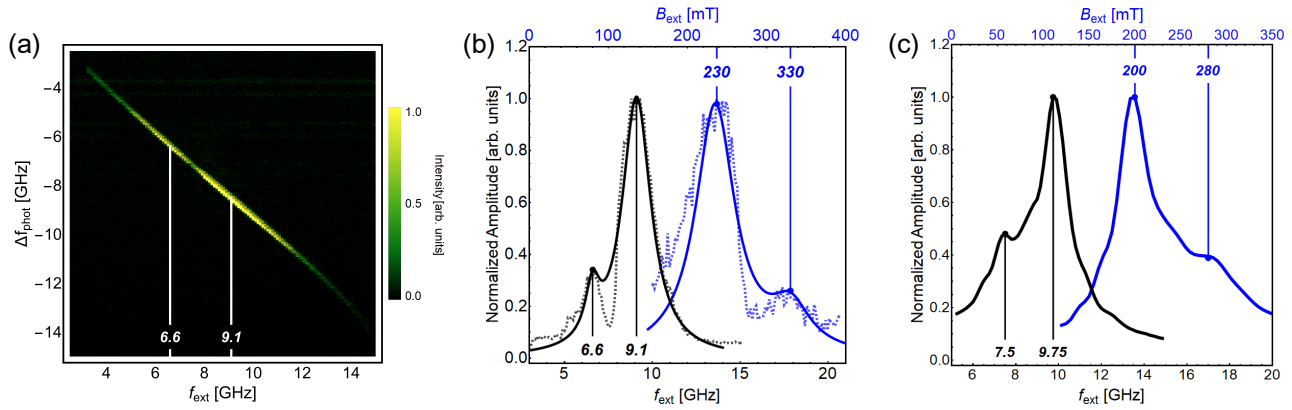

FIG. 2. (a) µBLS intensity measured at circularly structured MNP arrangement shown in the inset of Fig. 1 detected in an microwave excitation frequency range of $f_{ext} = 0$ GHz to 15 GHz as a function of the external excitation frequency f_{ext}. The data were recorded at an external field strength of $B_{ext} = 230$ mT. Integrating the data for each f_{ext} leads to an accumulated spectrum as shown in (b) (black dashed curve). It is clearly visible, that one main signal is present at $f_{ext} = 9.1$ GHz, accompanied by a satellite signal located at $f_{ext} = 6.6$ GHz. Keeping the excitation frequency constant at $f_{ext} = 9$ GHz and sweeping the external field strength yields the corresponding accumulated field-dependent spectrum which also exhibits two signals (blue dashed curve). The continuous curves represent fits with two Lorentz curves to the corresponding data. (c) Simulated f_{ext}- (black curve) and B_{ext}-dependent spectra (blue curve) of a hexagonally arranged, circularly shaped MNP assembly. The assembly had a diameter of 300 nm. The frequency-dependent spectrum was calculated for $B_{ext} = 200$ mT, while the external field strength dependent spectrum was simulated for $f_{ext} = 9.75$ GHz. Both spectra show a main peak accompanied by a satellite peak of lower intensity.

an external microwave of a defined excitation frequency f_{ext}. The impinging laser photons can then interact with the magnetic excitations, which causes a frequency shift Δf_{phot} by inelastic scattering (Brillouin process). This frequency shift Δf_{phot} represents a distinct signature of the corresponding magnetic oscillation. Thus, measuring the intensity of the inelastically scattered photons for pairs of excitation frequency f_{ext} and frequency shift Δf_{phot} yields insight into the magnetic characteristics of the system at constant B_{ext}. Furthermore, instead of analyzing the f_{ext}-dependent response of the magnetic structure at a constant magnetic field strength B_{ext}, B_{ext}-dependent properties can also be examined for constant f_{ext} by measuring the intensity of inelastically scattered photons versus Δf_{phot} at different external field strength B_{ext}. The frequency and static magnetic field dependent µBLS-experiments were performed at room temperature. All measurements were recorded in a excitation frequency range from $f_{ext} = 0$ GHz to 15 GHz and a magnetic field range from $B_{ext} = 100$ mT to 400 mT.

C. Theoretical Modelling

Micromagnetic modeling of the corresponding MNP-arrangements is indispensable for evaluating the results obtained from the µBLS-experiments, since the origin of the occurring signals is usually not entirely intuitive. To obtain deeper insight into the dynamic properties of such arrangements, a code has been developed for elucidating the associated characteristics. For details of this code, we refer the reader to our previous publications[27,28].

Since magnetite nanoparticles of diameters of less than 50 nm can be considered as single domain particles[29,30], each MNP can be represented by a single vector $\vec{m}_i(\vec{r}, t)$ (with $\vec{r}$ denoting the position vector and t the time) in the model. Each MNP carries a magnetic moment of $m = 2.2 \cdot 10^5\ \mu_B$, where μ_B is the Bohr magneton. A magnetic moment $\vec{m}_i(\vec{r}, t)$ interacts only via dipole-dipole interaction with its neighboring moments. Solutions of the time evolution of the whole magnetic system $\vec{M}(\vec{r}, t) = \sum_i \vec{m}_i(\vec{r}, t)$ under an external exciting microwave field $\vec{B}_{mw}(t, f_{ext})$ are then obtained by numerically integrating of the equation of motion described by the Landau-Lifshitz-Gilbert equation. The effective magnetic field acting on each nanoparticle is then calculated as a superposition of the dipolar contributions of all other magnetic moments $\vec{B}_{dd}$, the static external field $\vec{B}_{ext}$, and the excitation field of the microwave $\vec{B}_{mw}(t, f_{ext})$. The corresponding theoretical µBLS-spectra are obtained by performing a Fourier transformation of the time-dependent magnetization of each particle $\vec{m}_i(\vec{r}, t)$ over 10 periods for each excitation frequency f_{ext} and external static field strength B_{ext} and subsequently integrating the corresponding amplitude A_{FT} over the whole structure.

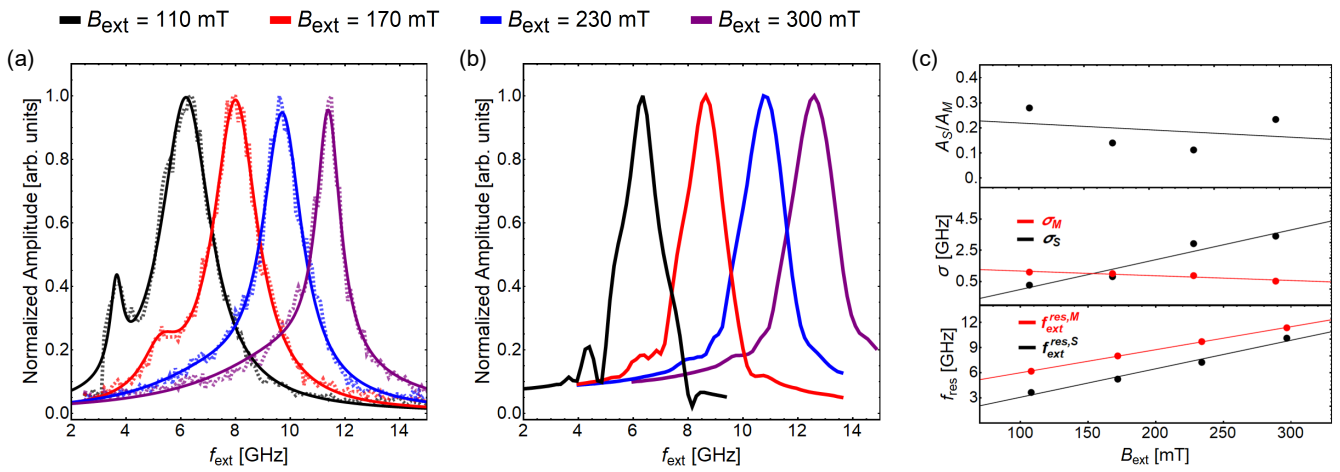

FIG. 3. (a) Integrated µBLS-spectra recorded at a non-structured, layered MNP-arrangement at different external field strengths B_{ext}. As f_{ext} increases, the resonance positions are shifted according to the resonance condition (see Eq. 1). The linewidths $\sigma_{\mathrm{S/M}}$ of the two resonances and the ratio of their intensities $A_{\mathrm{S}}/A_{\mathrm{M}}$ show distinct field dependencies, which are shown in (c). (b) Simulated frequency dependence of a non-structured, layered MNP-assemblies at different B_{ext}. While at low B_{ext} of 100 mT a satellite peak can be recognized, at large B_{ext} of 300 mT its presence is only noticeable as an asymmetry in the low frequency range of the spectrum.

III. RESULTS

A. Circularly shaped MNP arrangement

Figure 2 (a) shows a typical frequency dependent µBLS-specum as a color plot obtained from the circularly structured arrangement of MNPs shown in the inset of Fig. 1. The external static magnetic field strength was set to $B_{\mathrm{ext}} = 230$ mT in the sample plane. The intensity of the Brillouin-scattering signal is color coded, meaning that bright pixels correspond to a high scattering rate of the inelastically scattered laser photons. The frequency of the externally applied microwave-field f_{ext} is shown on the horizontal axis, and the frequency shift of the scattered light Δf_{phot} is shown on the vertical axis. A signal showing an excitation frequency dependence in the range between f_{ext} = -4 GHz and -12 GHz (Stokes-Signal) is clearly visible, which arises due to resonant excitations within the magnetic system. Integrating the intensities of all Δf_{phot} for each f_{ext}, i.e., each vertical line of the color plot is summed up, leads to an integrated µBLS spectrum as shown in Fig. 2 (b) (black dashed curve). The other spectrum (blue dashed curve) is obtained by a magnetic field sweep at constant f_{ext} and will be discussed in more detail below. Note that the two spectra shown in Fig. 2 (b) belong to two different abscissas as indicated in the figure. In the following only integrated spectra of these two types will be considered, since they contain all the relevant information.

First, we consider the f_{ext}-dependent measurement in Figure 2 (b), it is clearly visible, that in addition to the main signal a satellite resonance with lower intensity can be identified. Fitting the integrated µBLS-spectrum with two Lorentz curves (black continuous curve), the resonance frequency of the main peak located at $f_{\mathrm{ext,M}}^{\mathrm{res}} = 9.1$ GHz and of the satellite peak located at $f_{\mathrm{ext,S}}^{\mathrm{res}} = 6.6$ GHz can be extracted. The resonance condition for each MNP is given by

$$\begin{aligned} \frac{\omega_{\mathrm{ext}}}{\gamma} &= B_{\mathrm{eff}}^{\mathrm{res}} \\ &= B_{\mathrm{ext}}^{\mathrm{res}} + B_{\mathrm{int}}, \end{aligned} \tag{1}$$

where $B_{\mathrm{eff}}^{\mathrm{res}}$ denotes the effective local magnetic field at resonance, ω_{ext} ($= 2\pi f_{\mathrm{ext}}$) the angular excitation frequency of the microwave field, $\gamma = ge/2m$ the gyromagnetic ratio, g the Landé-factor, e the elementary charge, and m the mass of the electron. The effective local magnetic field at resonance is given as the sum of the external magnetic field at resonance $B_{\mathrm{ext}}^{\mathrm{res}}$ and the internal magnetic field B_{int} due to the dipolar interaction with neighboring MNPs. Typically, in these structures the component of B_{int} parallel to $B_{\mathrm{ext}}^{\mathrm{res}}$ is smaller at the edges than in the center of the structure[27]. As all MNPs involved are of the same species, the two signals must arise from MNPs experiencing different local effective magnetic fields. Taking into account that the local effective magnetic field acting on an MNP is the superposition of the external magnetic field and the local dipole field B_{dd}, the two resonances can be attributed to MNPs residing in different local environments within the arrangement. It can be concluded, that the satellite peak arises from locations with lower dipole fields which lead to lower resonance frequencies than that of the main peak. This is a strong indication that the satellite peak originates from the edges of the MNP arrangement, while the main signal can be interpreted as a resonant excitation of the bulk of

the system.

In addition to the f_{ext}-dependent measurement, the blue curves in Fig. 2 (b) show a external field dependent spectrum recorded at a constant excitation frequency $f_{\mathrm{ext}} = 9$ GHz with its corresponding fit. As f_{ext} is kept constant and a sweep of the external static field B_{ext} is performed, the main peak will occur at lower B_{ext} compared to the satellite peak. This can be understood on the basis of the resonance condition (equation 1). Exciting the magnetic system with a constant f_{ext} will lead to a constant resonance field $B_{\mathrm{eff}}^{\mathrm{res}}$. Areas which experience smaller dipole fields such as the edges will be in resonance at higher external fields $B_{\mathrm{ext}}^{\mathrm{res}}$ than those with larger dipole fields such as the center of the structure. As a result the main peak, which is attributed to the central region of the structure, will appear first in the spectrum. Although the shape of the spectrum is slightly changed, the resonance fields of the satellite and the main peak of $B_{\mathrm{ext,S/M}}^{\mathrm{res}} = 330$ mT and 230 mT are in good agreement with the results of the frequency dependent measurements, i.e. fulfilling equation 1 with the corresponding parameters.

In order to underline the experimental findings, micromagnetic simulation were carried out for a model system to analyse the f_{ext} and B_{ext}-dependent properties of the circularly structured MNP-arrangement in Fig. 1. The model system comprises one layer of MNPs arranged to a circle with a diameter of 300 nm. Within the circle the MNPs are hexagonally arranged, i.e., densely packed. Fig. 2 (c) shows the simulated f_{ext}- (black curve) and B_{ext}-dependent spectra (blue curve) of the circularly shaped model arrangement. The f_{ext}-dependent spectrum is calculated for an external field strength of $B_{\mathrm{ext}} = 200$ mT. Similar to the µBLS-measurement in Fig. 2 (b), the calculated µBLS spectrum also shows two peaks. The main peak is located at a resonance frequency of $f_{\mathrm{ext,M}}^{\mathrm{res}} = 9.75$ GHz, and the satellite peak at $f_{\mathrm{ext,S}}^{\mathrm{res}} = 7.5$ GHz. Furthermore, the intensity of the satellite peak is lower with respect to the main peak, which reflects the characteristics deduced from the µBLS-experiments. Sweeping B_{ext} instead of f_{ext} and keeping the excitation frequency constant at 9.75 GHz, an external field dependent spectrum is calculated. As in the case of the B_{ext}-dependent experiment in Fig. 2 (b), a slightly changed shape of the modeled spectrum can be noticed, but the resonance positions of the main and the satellite peak at $B_{\mathrm{ext,M}}^{\mathrm{res}} = 200$ mT and $B_{\mathrm{ext,S}}^{\mathrm{res}} = 280$ mT are in good agreement with the resonance condition.

B. Non-structured, layered MNP arrangement

We will now compare the observed characteristics of a structured MNP arrangement with those of a non-structured one. In Fig. 3 (a), four f_{ext}-dependent spectra recorded at four different external field strengths of the non-structured MNP arrangement are shown as dashed curves. The spectrum taken at $B_{\mathrm{ext}} = 110$ mT (black curve) is considered first. The two resonances are again clearly visible in this spectrum at $f_{\mathrm{ext,S/M}}^{\mathrm{res}} = 3.6$ GHz and 6.2 GHz. When increasing B_{ext} from 110 mT to 170 mT (red curve), the characteristics of the spectral features changes. First, the resonance positions shift to higher f_{ext}, as a result of the altered resonance condition. Second, at the higher B_{ext} of 170 mT, the ratio of the intensities of the satellite peak with respect to the main peak $A_{\mathrm{S}}/A_{\mathrm{M}}$ is decreased compared to $B_{\mathrm{ext}} = 110$ mT. Furthermore, the linewidth of the satellite peak σ_{S} increases from $\sigma_{\mathrm{S}} = 0.3$ GHz to 0.8 GHz, while the linewidth of the main peak σ_{M} decreases from $\sigma_{\mathrm{M}} = 1.1$ GHz to 0.9 GHz. Further increasing of B_{ext} to 230 mT and 300 mT, shows that the trends for $f_{\mathrm{ext,S/M}}^{\mathrm{res}}$, $\sigma_{\mathrm{S/M}}$, and $A_{\mathrm{S}}/A_{\mathrm{M}}$ continue almost linearly up to 300 mT. Fitting the experimental spectra by two Lorentzian lines, the findings can be quantified. The results are summarized in Fig. 3 (c).

Comparing the spectrum of the circularly shaped MNP-arrangement in Fig. 2 (b) (black curve) and the spectrum of the non-structured, layered system at an external field strength of $B_{\mathrm{ext}} = 230$ mT in Fig. 3 (a) (blue curve), two differences can be observed. First, the resonance frequencies of the two samples are not the same and differ considerably despite the same type of MNPs forming the arrangements and the same external field strength used in the experiment. The resonance frequencies of the circularly shaped assembly are $f_{\mathrm{ext,S/M}}^{\mathrm{res}} = 6.6$ GHz and 9.1 GHz whereas, those of the non-structured, layered system are higher, i.e. frequencies of $f_{\mathrm{ext,S/M}}^{\mathrm{res}} = 7.2$ GHz and 9.7 GHz. The reason is the difference in size of the two arrangements. Smaller structures experience stronger dipole fields and thus lower resonance frequencies are required to fulfill the resonance condition. Second, the amplitude of the satellite peak A_{S} measured at the circularly shaped MNP-assembly is much larger compared to A_{S} of the non-structured system. This also results directly from the size of the assemblies. While in the larger non-structured system only a small fraction of the MNPs are located near the edges, a much larger fraction of MNPs are located close to the edge of the smaller circularly shaped assembly. This finding further confirms that predominantly MNPs close to the edges contribute to the satellite peak resonance.

To further analyze the observed characteristics at different B_{ext} of the non-structured layered MNP superlattice, a model system of sufficiently large lateral extension has been defined. This second model system consists of hexagonally arranged moments up to 8 layers high and a lateral extension of the entire system of 1 µm. To mimic the spectra more realistically, not all magnetic moments were incorporated in the Fourier transformation, since the area exposed to the photon beam during the µBLS experiments is only about 300 nm in diameter. Thus, only moments within a cylinder of 300 nm in diameter in the center of the system were included in the Fourier analyses. Fig. 3 (b) shows the simulated f_{ext}-dependent spectra which can be compared with the corresponding experimental data of Fig. 3 (a). The spectrum simulated at $B_{\mathrm{ext}} = 100$ mT possesses a main peak at f_{ext}

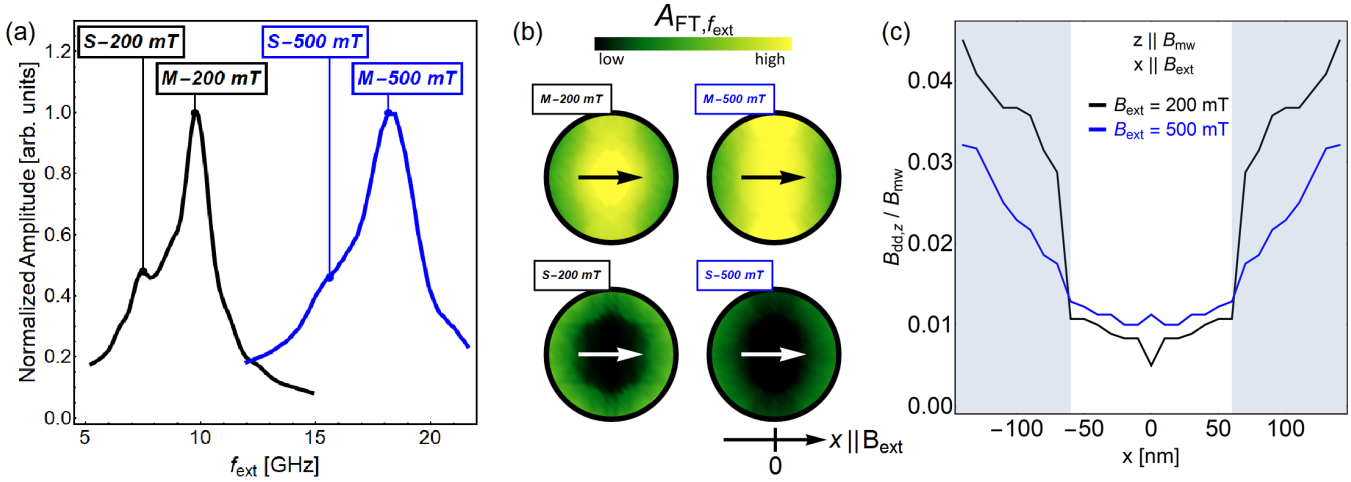

FIG. 4. (a) Simulated f_{ext}-dependent µBLS-spectra of a circularly shaped monolayer of MNPs with a radius of 150 nm. The spectra were calculated at B_{ext} = 200 mT (black curve) and 500 mT (blue curve). Increasing B_{ext} results in a shift of the resonance position according to the resonance condition (Eq. 1). In addition, a decrease of the intensity of the satellite peak with increasing B_{ext} is visible. (b) Performing 2D-Fourier-analyses unveils the active regions of the two resonances. As B_{ext} increases, the active areas of the satellite resonance decrease resulting in a reduction of its relative intensity, compared with the main resonance. The arrows indicate the direction of the external field pointing in the plane of the structure in x-direction. (c) Averaged dipole field $\vec{B}_{dd}$ in the direction of the external microwave $\vec{B}_{mw}$ over one period $T = 1/f_{ext}$ with f_{ext} = 7.5 GHz and 15.6 GHz (S-200 mT and S-500 mT). As the excitation is perpendicular to the plane of the structure, $\vec{B}_{mw}$ is parallel to the z-axis. The vertical axis is normalized to strength of the microwave field B_{mw} = 2 mT.

= 6.35 GHz accompanied by a satellite peak of lower intensity, located at f_{ext} = 4.4 GHz. Increasing the external field strength in the simulation leads to an increase of the resonance frequencies of both, main and satellite mode of the spectrum, until only an asymmetric signal remains in the low frequency range of the spectrum and the satellite and the main peak have merged, which is in good agreement with the observed characteristics from the µBLS-experiments. A possible explanation for these characteristics is that, as the external field strength increases, the angle between the external field and magnetic moments decreases, since their orientation is forced to align parallel to B_{ext}. As a result of the dipolar coupling between the magnetic moments, the corresponding dipole fields increase leading to a sharpening of the main peak. As a consequence, the frequency-range in which the particles resonate is reduced. Furthermore, as B_{ext} is increased, areas of high dipole fields located near the edges of the MNP arrangement will also be reduced in their lateral extensions. Thus, the intensity of the corresponding signal will also decrease and its linewidth will increase as the coupling to the central region becomes stronger. These findings will be analyzed in more detail in the next section, by considering the circularly shaped model system of a diameter of 300 nm again.

C. Influence of the external field strength on the different resonances

In Fig. 4 (a) simulations of two frequency dependent µBLS-spectra are shown. The simulations are based on the model system consisting of a single monolayer of MNPs shaped into a circular structure of a diameter of 300 nm. The spectra were derived for two different external field strengths of B_{ext} = 200 mT (black curve) and 500 mT (blue curve). The spectrum simulated at B_{ext} = 200 mT is the same as in Fig. 2 (c). As observed for the non-structured layered MNP arrangement, the resonance frequencies shift to higher frequencies, as the external field strength is increased. Furthermore, increasing B_{ext} results in a decrease of the ratio of the intensity of the satellite peak with respect to that of the main peak A_S/A_M. Deeper insight into the spectral features are obtained by analyzing the local activity within the magnetic structure at the corresponding resonance frequencies. Performing a two-dimensional Fourier transformation at the resonance fields of both spectra in Fig. 4 (a) the excitation pattern of the four resonances labeled M and S for 'main' and 'satellite' respectively, which are shown in Fig. 4 (b). The excitation pattern of the main resonances (M-200 mT and M-500 mT) clearly shows, that the main resonance originates from particles located in the center of the structure. The excitation patterns of the main resonance for the two different B_{ext} are very similar, except that the areas of highest activity are slightly larger for B_{ext} = 500 mT than for B_{ext} = 200 mT. Whereas the active regions of the main resonance is al-

most not affected by varying B_{ext}, the excitation pattern of the satellite resonance (S-200 mT and S-500 mT) shows a decrease of the active area with increasing B_{ext}. This explains the decrease of the ratio of the intensities $A_{\mathrm{S}}/A_{\mathrm{M}}$, since less particles near the edge of the structure contribute to the intensity of the satellite resonance with increasing B_{ext}. As the external field strength increases, the magnetic moment of each particle is forced to align with B_{ext}. As a consequence, the oscillation amplitude of each particle in the direction of the microwave field $\vec{B}_{\mathrm{mw}}$ denoted as the z-axis, i.e. perpendicular to the plane of the structure, decreases. Analyzing the dipole field caused by the mutual dipole interaction between the individual particles gives further insight into the observed characteristics. For this purpose, the dipole field B_{dd} acting on the particles is calculated over one period $T = 1/f_{\mathrm{ext}}$ of the microwave field for the resonances S-200 mT and S-500 mT with $f_{\mathrm{ext}} = 7.5$ GHz and 15.6 GHz respectively. Subsequently, the dipole fields of particles with the same r_x-value (meaning particles of the same column) are averaged and normalized to strength of the microwave field $B_{\mathrm{mw}} = 2$ mT. Figure 4 (c) shows the averaged z-component of the dynamic dipole field B_{dd} of each column of the model system as a function of the x-position of the column as indicated in the lower panel of Fig. 4 (b). As $B_{\mathrm{ext}} \parallel x$ increases from 200 mT (black curve) to 500 mT (blue curve), the averaged $B_{\mathrm{dd}} \parallel z$ near the edges of the structure decrease, whereas only slight variations in the center of the structure are observable. It follows that, as the external field strength increases, the difference of the averaged dipole field diminishes with respect to those of the center. Thus the capability to respond to the microwave field of MNPs near the edge of the structure decreases, which results in merging of the satellite resonance and the main resonance at high external field strengths.

IV. CONCLUSIONS

We investigated the dynamic response of hexagonally ordered, circularly structured MNP-arrangements utilizing µBLS-microscopy. It has been observed, that depending on the external conditions, two resonances appear in the spectra, which can be attributed to different areas within the magnetic system. While the main resonance originates from the central region, the observed satellite resonance is assigned to resonant particles near the edges of the system. Frequency dependent measurements were carried out at various external fields, revealing a distinct dependence on external field strength. Micromagnetic simulations unveiled the different characteristics of the dipolar coupling between the MNPs within the different locations of the arrangement. The dipolar coupling between the MNPs has a major impact on the lineshape of the µBLS spectra. Increasing the external field strength leads to a reduction the effective areas of lower internal magnetic fields, which leads to a reduction of the intensity of the corresponding satellite resonance compared to the main resonance. Thus, it has been demonstrated, that the response of the MNP arrangement is very sensitive to an external magnetic field and the frequency of the microwave excitation. A full understanding of these dependencies is essential for successfully incorporating structures into devices. In the future, we plan to extend our studies to higher frequency shifts of the scattered light. Such studies may then yield information about excitations of the exchange-coupled atomic magnetic moments within the individual MNPs.

[1] J.-H. Choi, H. Wang, S. J. Oh, T. Paik, P. S. Jo, J. Sung, X. Ye, T. Zhao, B. T. Diroll, C. B. Murray, and C. R. Kagan, Exploiting the colloidal nanocrystal library to construct electronic devices, *Science* **352**, 205 (2016)

[2] C.R. Kagan, E. Lifshitz, E.H. Sargent, and T.V. Talapin, Building devices from colloidal quantum dots *Science* **353**, 885 (2016)

[3] H. Zeng, C. T. Black, R. L. Sandstrom, P. M. Rice, C. B. Murray, and S. Sun, Magnetotransport of magnetite nanoparticle arrays, *Phys. Rev. B* **73**, 020402 (2006)

[4] C. Jiang, S. M. Ng, C. W. Leung, and P. W. T. Pong, Magnetically assembled iron oxide nanoparticle coatings and their integration with pseudo-spin-valve thin films, *J. Mater. Chem. C* **5**, 252 (2017)

[5] T. Paik, H. Yun, B. Fleury, S.-H. Hong, P.S. Jo, Y. Wu, S.-J. Oh, M. Cargnello, H. Yang, C.B. Murray, and C.R. Kagan, Hierarchical Materials Design by Pattern Transfer Printing of Self-Assembled Binary Nanocrystal Superlattices *Nano Letters* **17**, 1387 (2017)

[6] B.H. Zhou, and J.D. Rinehart, Pseudo Spin Valve Behavior in Colloidally Prepared Nanoparticle Films *ACS Appl. Elect. Mat.* **1**, 1065 (2019)

[7] K. Yakushiji, F. Ernult, H. Imamura, K. Yamane, S. Mitani, K. Takanashi, S. Takahashi, S. Maekawa, and H. Fujimori, Enhanced spin accumulation and novel magnetotransport in nanoparticles, *Nature Materials* **4**, 57 (2005)

[8] G. Song, M. Ranjbar, D. R. Daughton, and R. A. Kiehl, Nanoparticle-Induced Anomalous Hall Effect in Graphene, *Nano Letters* **19**, 7112 (2019)

[9] A. Dong, J. Chen, P.M. Vora, J.M. Kikkawa, and C.B. Murray, Binary nanocrystal superlattice membranes self-assembled at the liquid-air interface *Nature* **466**, 474 (2010)

[10] L. Giovannini, F. Montoncello, and F. Nizzoli, Effect of interdot coupling on spin-wave modes in nanoparticle arrays, *Phys. Rev. B* **75**, 024416 (2007)

[11] M.A. Boles, M. Engel, and D.V. Talapin, Self-assembly of colloidal nanocrystals: From intricate structures to functional materials *Chem. Rev.* **116**, 11220 (2016)

[12] A. Dong, J. Chen, . J. Oh, W. K. Koh, F. Xiu, X. Ye, D. K. Ko, K. L. Wang, C. R. Kagan, and C. B. Murray, Multiscale periodic assembly of striped nanocrystal superlattice films on a liquid surface, *Nano Letters* **11**, 841 (2011)

[13] E. Shevchenko, D.V. Talapin, N.A. Kotov, S. O'Brien, and C.B. Murray, Structural diversity in binary nanoparticle superlattices *Nature* **439**, 55 (2006)

[14] X. Ye, C. Zhu, P. Ercius, S.N. Raja, B. He, M.R. Jones, M.R. Hauwiller, Y. Liu, T. Xu, and P.A. Alivisatos, Structural diversity in binary superlattices self-assembled from polymer-grafted nanocrystals *Nature Comm.* **6**, 10052 (2015)

[15] S. Mamica, M. Krawczyk, M.L. Sokolovskyy, and J. Romero-Vivas, Large magnonic band gaps and spectra evolution in three-dimensional magnonic crystals based on magnetoferritin nanoparticles *Phys. Rev. B* **86**, 144402 (2012))

[16] F. Vernay, and H. Kachkachi, Single-particle versus collective effects in assemblies of nanomagnets: Screening *J. Mag. Mag. Mat.* **500**, 166286 (2020)

[17]B.W. Zingsem, T. Feggeler, A. Terwey, S. Ghaisari, D. Spoddig, D. Faivre, R. Meckenstock, M. Farle, and M. Winklhofer, Biologically encoded magnonics *Nat. Comm.* **10**, 4345 (2019)

[18]S. Tacchi, G. Gubbiotti, M. Madami, and G. Carlotti, Brillouin light scattering studies of 2D magnonic crystals, *J. Phys.: Condens. Matter* **29**, 073001 (2017)

[19]J. Chen, A. Dong, J. Cai, X. Ye, Y. Kang, J.M. Kikkawa, and C.B. Murray, Collective dipolar interactions in self-assembled magnetic binary nanocrystal superlattice membranes *Nano Letters* **10**, 5103 (2010)

[20]Z. Yang, J. Wei, P. Bonville, and M.-P. Pileni, Engineering the Magnetic Dipolar Interactions in 3D Binary Supracrystals Via Mesoscale Alloying *Adv. Funct. Mat.* **25**, 4908 (2015)

[21]M. Anand, J. Carrey, and V. Banerjee, Role of dipolar interactions on morphologies and tunnel magnetoresistance in assemblies of magnetic nanoparticles *J. Mag. Mag. Mat.* **454**, 23 (2018)

[22]H.T. Nguyen, and M.G. Cottam, Dipole-exchange spin waves in ferromagnetic nanostructures with spherical geometries *Surf. Rev. Lett.* **15**, 727 (2008)

[23]J. Pang, S. Xiong, F. Jaeckel, Z. Sun, D. Dunphy, and C. J. Brinker, Free-Standing, Patternable Nanoparticle/Polymer Monolayer Arrays Formed by Evaporation Induced Self-Assembly at a Fluid Interface, *J. Am. Chem. Soc.* **130**, 3284 (2008)

[24]A.V. Chumak, V.I. Vasyuchka, A.A. Serga, and B. Hillebrand, Magnon spintronics *Nature Physics* **11**, 453 (2015)

[25]Q. Wang, P. Pirro, R. Verba, A. Slavin, B. Hillebrand, and A.V. Chunmak, Reconfigurable nanoscale spin-wave directional coupler *Science Adv.* **4**, e1701517 (2018)

[26]T. Sebastian, K. Schultheiss, B. Obry, B. Hillebrands, and H. Schultheiss, Micro-focused Brillouin light scattering: imaging spin waves at the nanoscale, *Frontiers in Physics* **3**, (2015)

[27]N. Neugebauer, A. Fabian, M. Elm, D. M. Hofmann, M. Czerner, C. Heiliger, and P. J. Klar, Investigation of the dipole interaction in and between ordered arrangements of magnetic nanoparticles, *Phys. Rev. B* **101**, 104409 (2020)

[28]A. Fabian, M. Czerner, C. Heiliger, M. T. Elm, D. M.Hofmann, and P. J. Klar, Domain formation in rectangularmagnetic nanoparticle assemblies, *Phys. Rev. B* **98**, 054401 (2018)

[29]K.M. Krishnan, A.B. Pakhomov, Y. Bao, P. Blomqvist, Y. Chun, M. Gonzales, K. Griffin, X. Ji, and B.K. Roberts, Nanomagnetism and spin electronics: materials, microstructure and novel properties *J. Mater. Sci.* **41**, 793 (2006)

[30]S. Singamaneni, V. Bliznyuk, C. Binek, and E.Y. Tsymbal, Magnetic nanoparticles : recent advances in synthesis , self-assembly and applications *J. Mater. Chem.* **21**, 16819 (2011)